Title: Effect of metal loading on the CO_2 methanation: A comparison between alumina supported Ni and Ru catalysts

Authors: Adrián Quindimil, Unai De-La-Torre, Beñat Pereda-Ayo, Arantxa Davó-Quiñonero, Esther Bailón-García, Dolores Lozano-Castelló, José A. González-Marcos, Agustín Bueno-López, Juan R. González-Velasco

PII: S0920-5861(19)30308-6
DOI: https://doi.org/10.1016/j.cattod.2019.06.027
Reference: CATTOD 12274

To appear in: *Catalysis Today*

Received date: 16 January 2019
Revised date: 25 May 2019
Accepted date: 8 June 2019

Please cite this article as: Quindimil A, De-La-Torre U, Pereda-Ayo B, Davó-Quiñonero A, Bailón-García E, Lozano-Castelló D, González-Marcos JA, Bueno-López A, González-Velasco JR, Effect of metal loading on the CO_2 methanation: A comparison between alumina supported Ni and Ru catalysts, *Catalysis Today* (2019), https://doi.org/10.1016/j.cattod.2019.06.027

Effect of metal loading on the CO_2 methanation: A comparison between alumina supported Ni and Ru catalysts

Adrián Quindimil[a], Unai De-La-Torre[a], Beñat Pereda-Ayo, Arantxa Davó-Quiñonero[b], Esther Bailón-García[b], Dolores Lozano-Castelló[b], José A. González-Marcos[a], Agustín Bueno-López[b], Juan R. González-Velasco[a]*

[a]*Chemical Engineering Department, Faculty of Science and Technology, University of the Basque Country UPV/EHU, Barrio Sarriena, s/n, E48940 – Leioa, Bizkaia, Spain*

[b]*Department of Inorganic Chemistry, University of Alicante, Carretera de San Vicente s/n. E03080-Alicante, Spain.*

*Corresponding author: juanra.gonzalezvelasco@ehu.es (Juan R. González-Velasco)

Graphical abstract

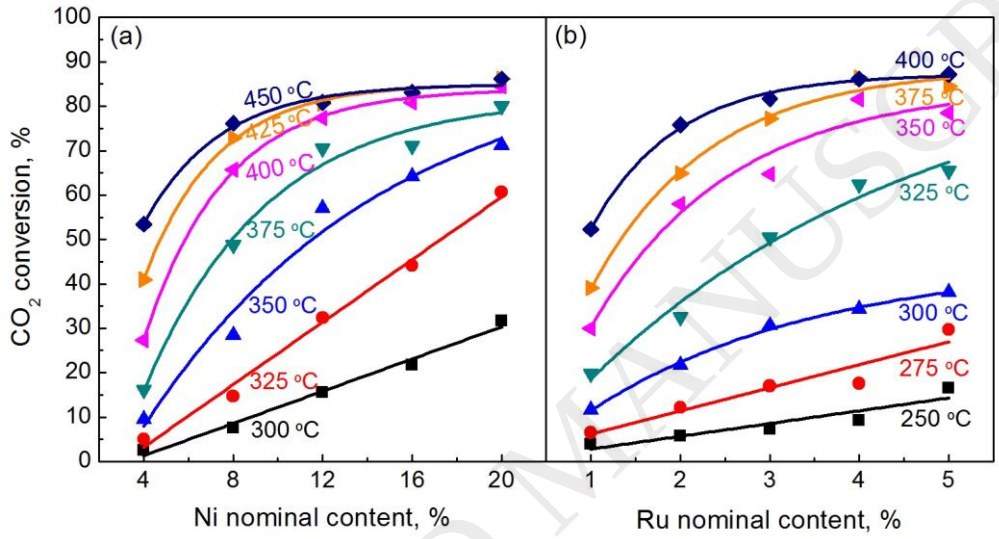

Highlights

- Increasing loading of Ni and Ru increases the surface basicity and forms new CO_2 adsorption sites.
- High calcination temperature leads to an increase of RuO_2 particle size and formation of inert Ni species.
- Ni/Al_2O_3 catalysts present high metal-support interaction, so that only a relative amount of metal is active for CO_2 methanation.
- Ru/Al_2O_3 catalysts are more efficient than Ni/Al_2O_3 in hydrogen dissociation; TOF of the former is about ten times than TOF of Ni catalysts.
- Optimal behavior was found for 12% Ni and 4% Ru, which provide metal surfaces of 5.1 and 0.6 $m^2\,g^{-1}$, respectively.

Abstract

The hydrogenation of CO_2 into CH_4 from H_2 produced by renewable energy is considered an interesting alternative in order to promote the development of such green energies. In the present work, the effect of Ni and Ru loadings on the catalytic performance of alumina-supported catalysts is studied for CO_2 methanation reaction. All catalysts were prepared by wetness incipient impregnation, characterized by several techniques (N_2-physisorption, CO_2-TPD, XRD, H_2-chemisorption, XPS and H_2-TPR) and evaluated for CO_2 methanation in a fixed bed

reactor at *GHSV* = 10,000 h^{-1} and $W / F^0_{CO_2}$ = 4.7 (g cat.) h mol^{-1}. Characterization results showed that addition of increasing loadings of Ni and Ru lead to the formation of both CO_2 adsorption and H_2 dissociation active sites, which are necessary to carry out CO_2 hydrogenation into methane. Easily reducible ruthenium was dispersed on γ-Al_2O_3 in form of large agglomerates, whereas Ni was better dispersed presenting a great interaction with the support. 12% Ni and 4% Ru resulted to be the optimal contents providing metal surfaces of 5.1 and 0.6 m^2 g^{-1}, T_{50} values of 340 and 310 °C and activity being quite stable for 24h-on-stream. In terms of turnover frequency (*TOF*), 4%Ru/Al_2O_3 catalyst was quite more efficient than 12%Ni/Al_2O_3, probably due to a greater ability of ruthenium to dissociate hydrogen. The apparent activation energies for alumina supported Ni and Ru were 129 and 84 kJ mol^{-1}, respectively.

Keywords: CO_2 methanation, metal loading, ruthenium, nickel, particle size

Nomenclature

d_p	Catalyst particle diameter, mm
d_{pore}	Mean pore diameter, nm
E_{ap}	Apparent activation energy, kJ mol^{-1}
F_i	Molar flow of component i, mol h^{-1}
GSVH	Gas hour space velocity, h^{-1}
$-r^0_{CO_2}$	Initial reaction rate, mol CO_2 h^{-1} (g cat.)$^{-1}$
R	Ideal gas constant, kJ mol^{-1} K^{-1}
S_{BET}	Specific surface, m^2 g^{-1}
S_{Me}	Metal surface, m^2 g^{-1}
T	Temperature, K
T_{50}	Temperature for 50% CO_2 conversion, °C
TOF	Turnover frecuency, s^{-1}
V_{meso}	Mesopore volume, cm^3 g^{-1}
W	Catalyst weight, g
$W / F^0_{CO_2}$	Space-time, (g cat.) h mol^{-1}
X_{CO_2}	Carbon dioxide conversion, %
Y_{CH_4}	Methane yield, %
Y_{CO}	Carbon monoxide yield, %

1. Introduction

Progressive reduction of carbon dioxide emissions, considered as a route to decrease the impact of greenhouse gases (GHG) on climate, is one of the major environmental challenges of today's society. The replacement of fossil energy by renewable energy sources is the best option to tackle that challenge. The main downside is that renewable energy such as wind and solar is fluctuating, i.e., in many cases, the power from electric generators does not match the energy demand. Besides, renewable energy power installed worldwide is far from enough to meet the global energy demand. Thus, the development and incorporation of alternative transition technologies into the current energy system is necessary [1].

In order to control CO_2 emissions and stabilize CO_2 atmospheric concentration, transition changes are needed in the current energy system. Nowadays, there are two main strategies: (i) CO_2 capture and storage (CCS) and (ii) CO_2 recycling. Although CCS technology is viable in reducing CO_2 emissions, it has some disadvantages such as the necessity of a site for CO_2 sequestration close to CO_2 source or the costly transportation of captured CO_2 to the storage site, which reduces the efficiency of the process [2]. Nevertheless, CO_2 recycling is considered a complementary and interesting alternative to CCS. Through this process, CO_2, the major atmospheric pollutant, can be converted into chemical compounds (mainly urea, salicyclic acid and polycarbonates) or fuels [2–4]. Considering that the amount of carbon emitted from fossil fuels combustion is 100 times higher than that used for synthesis of chemicals, it seems more reasonable to convert CO_2 into different energy vectors such as methane, methanol and dimethylether [4–7].

Among the different conversion alternatives, CO_2 methanation is thermodynamically the most favorable reaction. Carbon dioxide, captured from combustion or other processes, can be combined with H_2 generated from renewable energy and catalytically converted into methane or synthetic natural gas (SNG) according to the Sabatier reaction:

$$CO_2 + 4H_2 \rightarrow CH_4 + 2H_2O \qquad \Delta H = -165 \text{ kJ mol}^{-1} \qquad (1)$$

In that way, not only anthropogenic CO_2 emissions are reduced, but also surplus renewable energy is stored in form of SNG that could be easily transported by the current gas grid.

Generally, catalysts used in CO_2 methanation consists of group VIII transition metals (active phase) supported over mesoporous solids. γ-Alumina has proven to be an effective support to carry out CO_2 methanation [8, 9]. This support provides high specific surface area (100-250 m^2 g^{-1}), contains surface basicity (hydroxyl groups) for CO_2 activation and over which the active phase can be dispersed. Among group VIII metals, Ni and Ru have been the most used [10].

These metals, in their reduced state, are able to effectively dissociate the hydrogen that reacts with CO_2 adsorbed on the support. Ni-based catalysts have been extensively investigated because of their high activity and low price [11–15], whereas Ru-based catalysts due to their excellent activity and selectivity at low temperature [16–20]. Therefore, a catalytic component is required to activate CO_2 for a further reduction, as the aluminum oxide (Al_2O_3), and also a metal component (here Ni or Ru) that is able to dissociate H_2. Providing that both functionalities are present, activity, selectivity and deactivation of the catalyst seem to be significantly dependent on the metal particle size [14, 16]. It seems that Ni-based catalysts require high metal loadings and are easily deactivated by sintering or coke deposition, in a more extension than Ru based catalysts, which in turn are much more expensive. In some cases, a third promoter component is used to improve metal dispersion and CO_2 adsorption [18, 19, 21, 22] or to avoid fast deactivation by sintering and fouling [12, 23].

In recent literature, there are many works that report separately the catalytic performance of Ni-based and Ru-based formulations at different operation conditions, which makes a direct comparison between the activity of both metals difficult. Previously, Garbarino et al. [8] studied and compared the activation, catalytic performance and stability of commercial 3%Ru/Al_2O_3 and 20%Ni/Al_2O_3 catalysts, observing that the performance of the former was better than that of the latter. For this study, we have prepared both series of Al_2O_3-supported Ni and Ru catalysts with loadings that assure metal particle sizes to be effective to dissociate H_2 and activate CO_2 reduction. The aim is to compare the activity of supported Ni and Ru and to study the effect of metal loading.

2. Experimental

2.1 Catalysts preparation

In order to synthesize alumina-supported catalysts with different Ni and Ru contents, a simple, fast and well-known preparation method such as wetness incipient impregnation was used. This method consisted of adding the previously dissolved Ni or Ru precursor on a commercial γ-A_2O_3 *(Saint-Gobain NorPro 6173)* driving the solute into the pores by capillary forces. The employed metal precursors were $Ni(NO_3)_2{\cdot}6H_2O$ *(Sigma Aldrich, 99.99%)* and $Ru(NO)(NO_3)_3$ in diluted nitric acid *(Sigma Aldrich, Ru = 1.5% w/v).*

In total, 5 Ni-based catalysts were prepared varying the Ni nominal content from 4 to 20 wt.%. Firstly, a volume of $Ni(NO_3)_2{\cdot}6H_2O$ aqueous solution 1.2 times larger than catalysts pore volume was impregnated dropwise over Al_2O_3 (V_P = 0.6 $cm^3\ g^{-1}$). Secondly, the impregnated samples

were dried during 6 h at 60 °C and further 6 h at 120 °C. Finally, the catalysts were calcined at 500 °C for 4 h with a heating rate of 5 °C min^{-1}.

Regarding Ru-based catalysts, 5 additional samples were synthesized by successive impregnations, varying Ru loading from 1 to 5 wt.%. Due to Ru precursor solubility limitations, a maximum 1% of Ru was incorporated in each impregnation. In line with Ni based catalysts, $Ru(NO)(NO_3)_3$ solution volume 1.2 times greater than V_P was impregnated, after adjusting the pH of the solution to 1 by acid nitric addition. After each impregnation, samples were dried during 6 h at 60 °C followed by extra 6 h at 120 °C and calcined at 400 °C during 4 h with a heating rate of 1 °C min^{-1}. These calcination temperatures for Ni and Ru catalysts were previously optimized by thermodiffractometric studies varying the temperature from room temperature to 1000 °C, as the minimum temperature for decomposing each precursor.

2.2. Characterization techniques

N_2 adsorption-desorption. Textural properties of the samples were determined from N_2 adsorption-desorption isotherms measured at -196 °C using a *Micromeritics TRISTAR II 3020* instrument. Pore volumes were calculated by t-plot method while pore size distribution of mesoporous solids was determined using BJH method. The samples were previously degassed overnight under N_2 flow.

CO_2 Temperature Programmed Desorption (CO_2-TPD). Surface basicity and basic sites distribution were analyzed by TPD-MS studies. Micromeritics AutoChem 2920 instrument was used coupled to a *MKS Cirrus* mass spectrometer. First of all, Ni/Al_2O_3 and Ru/Al_2O_3 catalysts were reduced under 5%H_2/Ar flow for 60 min at 500 °C and 30 min at 300 °C, respectively. Then, CO_2 adsorption step was performed at 50 °C by feeding 50 cm^3 STP/min of 5%CO_2/He flow until saturation. Thereafter, the samples were flushed out with helium for 60 min to remove weakly adsorbed CO_2 from the surface. Finally, desorption was carried out from 50 to 850 °C with a heating rate of 10 °C min^{-1}. The CO_2 desorption was continuously monitored with a mass spectrometer.

X-Ray Diffraction (XRD). Crystalline phases of alumina supported Ni and Ru catalysts were identified by XRD on a PANalytical Xpert PRO diffractometer with Cu kα radiation (λ = 1.5418 Å) and Ni filter. The operating conditions were 40 kV and 40 mA and diffractograms were recorded from 5 to 70° 2θ with 0.02° per second sampling interval. PANalytical X'pert HighScore specific software was used for data treatment and JCPDS database was used to interpret the diffractograms. On the other hand, the thermodifractometric studies were carried out in a Bruker D8 Advance diffractometer operating at 30 kV and 20 mA, equipped with a Cu tube (λ =

1.5418 Å), a Vantec-1 PSD detector, and an Anton Parr HTK2000 high-temperature furnace. The powder patterns were recorded in 2θ steps of 0.033° in the 15 ≤ 2θ ≤ 70 range, counting for 2 s per step (total time for each temperature was 1 h). Data sets were recorded from 30 to 1010 °C every 20 °C with 5 °C min^{-1} heating rate.

Hydrogen chemisorption. The dispersion of active sites was measured by H_2 chemisorption employing a Micromeritics ASAP 2020 apparatus. Prior to the experiments, Ni/Al_2O_3 and Ru/A_2O_3 catalysts were reduced with pure H_2 for 2 h at 500 °C and 350 °C, respectively. After that, the samples were degasified at the same temperature for 90 min. For both formulations, the adsorption isotherms were recorded at 35 °C varying the pressure between 50 and 450 mmHg. Adsorption stoichiometries of Ni/H = 1 and Ru/H = 1 were assumed.

Hydrogen Temperature Programmed Reduction (H_2-TPR). The reducibility of Ni/Al_2O_3 and Ru/Al_2O_3 catalysts was studied by H_2-TPR tests. The experiments were performed on a *Micromeritics AutoChem 2920* instrument. In the case of Ni/Al_2O_3, these were firstly pre-treated at 350 °C for 30 min under Ar flow in order to remove adsorbed H_2O and CO_2. The reducing gas flow was 50 cm^3 STP/min of 5%H_2/Ar and the temperature was increased from 30 to 900 °C with a heating rate of 10 °C min^{-1}. The water formed during reduction was trapped using a cold trap and the hydrogen consumption was continuously monitored with a TCD detector.

X-Ray Photoelectron Spectroscopy. The catalysts were characterised before and after the catalytic tests. X-ray photoelectron spectroscopy (XPS) analysis was performed by using a K-Alpha spectrophotometer (Thermo-Scientific) with a high-resolution monochromator. The binding energy was adjusted using the C 1s transition, appearing at 284.6 eV. Binding energy values measured are accurate to ±0.2 eV. Oxidation states of Ni and Ru, as well as, surface atomic composition were determined by means of this technique.

2.3. CO_2 methanation experiments

CO_2 methanation reactions were performed in a downflow fixed bed reactor (D_{in} = 9 mm) and the product distribution was analyzed with a gas chromatograph (*Agilent 490 micro GC*). Ni and Ru based catalysts were first reduced for 1 h under 20%H_2/He flow (300 cm^3 STP/min) at 500 °C and 300 °C, respectively. After cooling down to 200 °C in inert gas, the reaction mixture was fed to the reactor with a 5:1:1.5 H_2:CO_2:He molar ratio. The catalytic performance of the prepared catalysts was studied between 200 and 500 °C, in steps of 25 °C, with a heating rate of 5 °C min^{-1} between each step. The He, H_2, CO_2, CH_4 and CO concentrations at the reactor exit were monitored once steady state was reached.

Activity tests were carried out at atmospheric pressure with 0.5 g of catalyst (d_p = 0.3-0.5 mm). The catalyst particles were diluted to 50% with quartz particles in order to improve heat transfer. In these conditions, *GHSV* and $W / F_{CO_2}^0$ were 10,000 h^{-1} and 4.67 (g cat.) h mol^{-1}, respectively. Additionally, the effect of space time ($W / F_{CO_2}^0 = 0$) on CO_2 conversion was studied varying space velocity from 10,000 h^{-1} to 40,000 h^{-1} at different reaction temperatures.

CO_2 conversion (X_{CO_2}), CH_4 yield (Y_{CH_4}) and CO yield (Y_{CO}) were calculated as:

$$X_{CO_2} = \frac{F_{CO_2}^{in} - F_{CO_2}^{out}}{F_{CO_2}^{in}} \times 100 \quad (2)$$

$$Y_{CH_4} = \frac{F_{CH_4}^{out}}{F_{CO_2}^{in}} \times 100 \quad (3)$$

$$Y_{CH_4} = \frac{F_{CO}^{out}}{F_{CO_2}^{in}} \times 100 \quad (4)$$

Activity of catalysts is also compared by T_{50}, which represents the temperature at which the catalyst achieves CO_2 conversion of 50% ($X_{CO_2} = 50\%$).

3. Results

3.1. Characterization

3.1.1. Surface properties

Figure S1 shows the N_2 physisorption isotherms as well as the pore size distribution of alumina support used for the prepared catalysts. As it can be noticed, the shape of the isotherms is characteristic of mesoporous solid: a great quantity of N_2 is adsorbed at intermediate relative pressures by multilayer filling with a hysteresis loop at relative pressures higher than 0.65 (type IV isotherm and H2 hysteresis loop according to IUPAC). Specific surface area, mesopore volume and average pore size values for fresh γ-Al_2O_3, compiled in Table 1, present values of 214 $m^2 g^{-1}$, 0.563 $cm^3 g^{-1}$ and 10.1 nm, respectively, which are high enough to perform the impregnation of large metal loading, allowing the present study concerning the effect of active phase loading.

FIGURE S1

Textural properties of alumina-supported Ni and Ru catalysts are also summarized in Table 1. As it can be noticed, the raise of Ni content from 4 to 20% leads to a gradual decrease of specific surface area and mesopore volume from 214 $m^2 g^{-1}$ to 131 $m^2 g^{-1}$ and from 0.563 $cm^3 g^{-1}$ to 0.326

cm^3 g^{-1}, respectively. These changes in textural properties are attributed to partial blockage/filling of alumina mesopores with NiO aggregates and/or to partial collapse of the mesoporous structure [11, 14, 24]. On the other hand, similar trends are observed when varying Ru loading.

TABLE 1

Additionally, the effect of Ni and Ru incorporation on the surface basicity was studied by means of CO_2-TPD. Figure 1 shows the CO_2-TPD profiles for γ-Al_2O_3 and for the catalysts with the highest contents of Ru and Ni, i.e., 5%Ru/Al_2O_3 and 20%Ni/Al_2O_3. As it can be observed, the prepared samples contain different CO_2 adsorption sites with different strength. According to desorption temperature or chemical bond strength, basic sites can be classified into weak (T < 150 °C), medium (T = 150-350 °C) and strong (T > 350 °C) [14, 25]. On the one hand, it can be observed that bare alumina presents a single desorption peak at 105 °C, attributed to CO_2 desorption from weak Bronsted OH^- groups [26]. On the other hand, the new CO_2 desorption peaks observed for 20%Ni/Al_2O_3 and 5%Ru/Al_2O_3 catalysts indicate that Ni and Ru addition leads to the formation of new basic sites with different strength. 20%Ni/Al_2O_3 presents a new CO_2 desorption peak at 275 °C, associated with decomposition of bidentate carbonate from medium-strength basic sites [15], whereas 5%Ru/Al_2O_3 catalyst shows a CO_2 desorption peak at 425 °C, attributed to decomposition of monodentate carbonate from strong basic sites [27]. The CO_2 surface density quantification obtained from integration of MS 44 signal is also shown in Table 1. While the CO_2 surface density of bare alumina is 0.32 µmol m^{-2}, the addition of increasing contents of Ni and Ru rises this value up to 0.5 and 0.42 µmol m^{-2}, respectively. Therefore, it can be concluded that Ni and Ru impregnation not only results in the formation of new type of basic sites, but also in an increase of surface basicity.

This increase of surface basicity with addition of both Ni and Ru could also theoretically be explained in terms of electronegativity. The electronegativity values of the elements that participate in CO_2 adsorption are 1.6, 1.9, 2.3 and 3.5 for Al, Ni, Ru and O, respectively. These values indicate that surface O^{2-} and OH^- groups linked to Al must contain higher negative charge density (lower basicity) than those attached to Ni and Ru. Thus, differences in electronegativity show that the involved 3 metals transfer negative charge density to surface O^{2-} following the sequence: Al > Ni > Ru. Therefore, considering that CO_2 is an acid gas with a high negative charge density, the sites with the highest CO_2 adsorption capacity (and the lowest negative charge density) correspond to O^{2-} (and OH^- if applicable) linked to Ru, followed by those linked to Ni and finally those bound to Al.

FIGURE 1

3.1.2. Crystallinity and metallic dispersion

Crystalline phases of reduced catalysts were identified by X-ray diffraction. XRD patterns of alumina supported catalysts with increasing Ni and Ru contents are shown in Figures 2a and 2b, respectively.

FIGURE 2

In all cases, XRD peaks can be observed at 37.7, 45.8 and 66.8° 2θ, corresponding to gamma-alumina (311), (400) and (440) diffraction planes, respectively (PDF 01-079-1558). These broad peaks together with an elevated XRD signal background point out that this γ-Al_2O_3 is rather an amorphous than a crystalline solid, which makes the identification of crystalline nano-particles more difficult due to peaks overlapping. In fact, for Ni/Al_2O_3 catalysts, the presence of crystalline Ni phases was only detected for catalysts with Ni contents higher than 8%. NiO was identified for calcined catalysts [9] (Figure S2) and the appearance of XRD peaks at 44.3, 51.7 and 76.1° 2θ revealed the formation of elemental Ni in reduced catalysts [12]. However, the presence of $NiAl_2O_4$ (peaks located at 37.0, 45.0 and 65.5° 2θ) could not be identified, since it contains the same spatial group with a similar cell parameter of Al_2O_3 (PDF 00-010-0339).

Both crystallite sizes and Ni dispersion are summarized in Table 2. The XRD patterns of catalysts with Ni content lower than 12% showed similar diffraction pattern to original Al_2O_3 (not shown), probably due to a high dispersion of Ni species (crystallite sizes lower than 5 nm). Therefore, Ni crystallite sizes could be only estimated by Scherrer equation for 12, 16 and 20% Ni loaded catalysts. In all cases, Ni crystallite sizes lower than the average pore size of Al_2O_3 (10.1 nm, see Table 1) were observed, which suggests that Ni could be located inside the pores of the catalytic support. It can be observed that dispersion values obtained by H_2-chemisorption match with the trend observed by XRD: the Ni crystallite size estimated by XRD grows from <5 to 7.3 nm, whereas dispersion is reduced from 38 to 11% with the increase of Ni loading. As will be seen later not all nickel can be reduced or is activated after reduction pretreatment for 1 h at 500 °C and therefore, we refer to the dispersion of nickel reducible at those conditions.

In the case of Ru/Al_2O_3 catalysts, diffraction peaks at 28.0, 35.1 and 54.2° 2θ were observed in calcined catalysts, characteristic of tetragonal RuO_2 [18, 19] (Figure S2). After reduction pretreatment at 300 °C, new XRD peaks were detected at 38.4, 42.2 and 44.0° 2θ confirming the presence of ruthenium in reduced state (PDF 00-006-0663). As it can be clearly observed, the intensity of the peaks grows with the increase of ruthenium content from 1 to 5%. The markedly more intense XRD peaks of hexagonal Ru compared to those of cubic Ni are due to higher

crystallinity and crystallite sizes, which have also been estimated by Scherrer equation and values are also summarized in Table 2. Note that Ru crystallite size increases from 7.4 to 12.1 nm, suggesting a small decrease in active phase dispersion. This trend is in line with H_2 chemisorption results: Ru dispersion slightly decreases from 5.5 to 3.9% as metallic content increases from 1 to 5%. Then, the lowest dispersion of 5%Ru/Al_2O_3 catalyst may be associated with the presence of larger Ru particles formed by agglomeration of several Ru nano-crystals.

TABLE 2

In order to determine the effect of temperature on the crystallinity of Ni/Al_2O_3 and Ru/Al_2O_3 samples, additional thermodiffractometric studies were done. Figure 3a shows a waterfall of XRD patterns of 12%Ni/Al_2O_3 catalyst measured between 30 and 1010 °C. The variations in intensity and position of the diffraction peaks with temperature are related to changes in the sample crystallinity or to the formation/disappearance of crystalline nickel phases. In fact, the unique peaks that remain unchanged in the whole temperature range are those assigned to inevitable diffraction of the platinum sample holder, at 39.7, 46.2 and 67.4° 2θ. Note that the color of the sample changed with temperature following this sequence: from gray to greenish-gray, from greenish-gray to greenish-blue and from greenish-blue to blue. In the 30 - 310 °C temperature range, only the characteristic XRD peaks of Al_2O_3 were detected, suggesting that higher temperature is needed for the formation of Ni crystalline phases. However, from 310 to 610 °C the development of a broad band can be observed at 62.9° 2θ, which is tentatively attributed to highly dispersed greenish-gray NiO. Finally, above 610 °C NiO characteristic peaks disappearance is detected, followed by the formation of more intense peak at 59.7° 2θ, assigned to blue $NiAl_2O_4$ [27, 28], being more crystalline than highly dispersed NiO. Note that above 710 °C, the peak at 37° 2θ gains in intensity, as a result of $NiAl_2O_4$ spinel formation contribution. Therefore, it seems that the formation of spinel takes place at temperatures above 600 °C and considering that Ni/Al_2O_3 samples were calcined at 500 °C, the presence of considerable amount of $NiAl_2O_4$ in the prepared catalysts seems unlikely.

FIGURE 3

On the other hand, the XRD patterns waterfall of 3%Ru/Al_2O_3 catalyst is shown in Figure 3b. In this case, the presence of Ru crystalline phase (RuO_2) is detected at temperatures above 230 °C and the XRD intensity at 28, 35 and 54.2° 2θ clearly rises with temperature up to 800 °C indicating the increasing formation of RuO_2 tetragonal nano-crystals. At temperatures between 810-1010 °C, however, the XRD intensity significantly drops, which indicates the disappearance of RuO_2 probably due to the formation of volatile oxides (RuO_X) [17]. Noteworthy, the size of the

nano-crystals remains stable (≈ 20 nm) up to 500 °C and afterwards exponentially grows until 60 nm, suggesting a notable decrease of Ru dispersion for temperatures above 500 °C. Therefore, this confirms that the calcination temperature of 400 °C seems to be enough to form crystalline RuO_2 as Ru precursor and avoid an excessive growing of the crystallites.

3.1.3. Analysis of Ni and Ru species nature by XPS and H_2-TPR

In order to study the atomic surface composition of prepared catalysts and the nature of surface Ni and Ru species, XPS characterization was carried out. A certain amount of carbon, attributed to atmospheric CO_2 adsorption, was detected by XPS on the surface of all catalysts (between 12 and 15%). Therefore, a direct analysis of the quantitative results of the surface composition is complex and more relevant information is obtained by analyzing the ratio of concentrations between elements. Figures 4a and 4b show the effect of metal loading on surface Ni/Al and Ru/Al atomic ratios of fresh and used (catalytically tested) samples. It should be noted that auxiliary lines in both Figures display a proportional evolution of Ni/Al and Ru/Al with metallic contents, i.e., considering that metallic content does not affect the dispersion.

FIGURE 4

In Figure 4a, it can be observed that in both cases the amount of surface Ni increases with the total amount of Ni. However, the surface Ni/Al ratios are below the auxiliary line, which suggests a certain decrease in Ni dispersion (see Figure 4a). These results are consistent with XRD results, where an increase of Ni particle size with the metal loading was observed. Note that the Ni/Al ratios are lower in the used catalysts compared to the fresh ones, indicating sintering during the catalytic tests. The impregnation of different amounts of Ru, however, has a different effect on Ru/Al surface atomic ratio (see Figure 4b). In this case, the amount of surface Ru also increases with Ru content; but unlike the Ni/Al ratios, the Ru/Al ratios follow the auxiliary line. This indicates that Ru dispersion does not vary considerably with the increase of metal loading from 1 to 5%. In fact, similar particle sizes of Ru were observed by H_2-chemisorption indicating the same trend. Finally, observe that the Ru/Al ratios are similar in fresh and in used catalysts, i.e., Ru dispersion remains stable during reaction, except for the 5% Ru sample.

Figures 5a and 5b show X-ray photoelectronic spectra corresponding to the nickel $2p_{3/2}$ transition for fresh and used Ni/Al_2O_3 catalysts, respectively. Deconvolutions of spectra were carried out, since in all cases broad and asymmetric bands were observed, suggesting the presence of different Ni species on the surface. Additionally, dashed black auxiliary lines were included in the graphs, which indicate the energies described in the literature for different nickel species. [29, 30]

FIGURE 5

All these catalysts exhibit peaks close to 856.0 and 858.0 eV with its corresponding shake-up satellites at ~862.0 and ~864.5 eV. Note that the first peak is located among 853.9 and 857.0 eV, binding energies assigned to bulk NiO and $NiAl_2O_4$, respectively [31]. From this observation, we can discard the presence of great amount of bulk NiO on all catalysts. The main peak at 856 eV corresponds to Ni^{2+} interacting with alumina [32], while the smaller peak at 858 eV is consistent with the formation of nickel spinel $NiAl_2O_4$ [28]. On the one hand, the slight shift of the main peak towards higher BE with the increase of Ni content could be due to the weakening of metal-support interaction [33]. On the other hand, the main peak remains in the same position after reaction, indicating that Ni species are stable during catalytic tests. It should also be mentioned that no Ni^0 specie was found in used catalysts (Figure 5b), since its passivation occurs when the samples are in contact with air.

Ru $3d_{5/2}$ core level XPS spectra of fresh and used Ru/Al_2O_3 catalysts are displayed in Figures 6a and 6b, respectively. As in the case of Ni catalysts, auxiliary dashed black lines indicating reported energies of different Ru species were included in the figures. XPS spectra of fresh catalysts with different content of Ru can be deconvoluted into two contributions assignable to two species of Ru, both cationic, at ~282.3 and ~280.8 eV. These peaks are consistent with the presence of Ru(VI) and Ru(IV) oxides on the surface of the catalysts [34, 35]. The XPS spectra of used catalysts exhibit the partial reduction of ruthenium oxides during the catalytic tests, showing two peaks at ~281.4 and ~280.0 eV. In this case, these peaks correspond to hydrated RuO_2 and metallic Ru, respectively [36, 37]. Finally, the long tail observed at binding energies higher than 282 eV is due to overlap with C 1s transition.

FIGURE 6

H_2-TPR experiments were carried out in order to analyze the reduction state of Ni and Ru species dispersed on alumina but also to determine the effect of metal loading over the reducibility of the prepared catalysts. Figures 7a and 7b show H_2-TPR profiles of fresh Ni/Al_2O_3 and Ru/Al_2O_3 catalysts, respectively. First of all, differences in redox properties are evident: the complete reduction of nickel-based catalyst is only achieved by increasing the temperature up to 900 °C, whereas only 250 °C are required for ruthenium loaded catalysts. These distinct redox properties could be translated in different catalytic performances, since it is well known that both active sites (Ni or Ru) must be reduced to carry out the hydrogenation of CO_2 efficiently.

FIGURE 7

With the aim of characterizing the type of nickel and ruthenium species presented in alumina supported catalysts, H_2-TPR profiles were deconvoluted applying Gaussian-type deconvolution. H_2-TPR profiles displayed in Figure 7a present 3 deconvoluted H_2 consumption peaks assignable to three different Ni species, named α, β and γ [14, 33, 38]. The peak located at the lowest temperature, close to 550 °C, is attributed to reduction of α-type NiO, weakly interacting with alumina. The second peak centered at 670 °C, however, is assigned to reduction of β-type NiO with stronger interaction with the support [28, 39]. Finally, the peak at the highest temperature, with maximum located close to 780 °C, is assigned to reduction of γ-type Ni specie forming well dispersed $NiAl_2O_4$ structure, in line with the results observed by thermo XRD study and XPS. Note that, in accordance with previous XPS results, H_2-TPR profiles shift to lower temperatures with increasing of Ni content, which is related to weakening of metal-support interaction already reported by other authors [24].

Relative amounts of Ni species together with reducibility percentages and H_2/Ni ratios are summarized in Table 3. Note that the relative amount of α-type NiO grows progressively with Ni loading, increasing from 8% (4%Ni/Al_2O_3) up to 44% (20%Ni/Al_2O_3), whereas the amount of γ-type NiO decreases from 62 to 14%. Additionally, in order to determine the amount of nickel reducible at 500 °C, additional H_2-TPR tests were run up to 500 °C, for 1 h and under 20% H_2/Ar (TPR profiles included in Figure S3). As expected, the percentage of nickel reducible at 500 °C increased from 10 to 56% with Ni loading, confirming the mentioned slight weakening of metal-support interaction and indicating that in no case will all nickel be reduced during reaction. Finally, note that the H_2/Ni ratio is close to 1 in all cases, which indicates, as previously observed in XPS characterization, that Ni^{2+} is the only specie reducible, according to the following reduction step: $NiO + H_2 \rightarrow Ni + H_2O$.

TABLE 3

Figure 7b shows deconvoluted H_2-TPR profiles of Ru/Al_2O_3 catalysts. All catalysts exhibit a main H_2 consumption peak with a maximum located at 210 °C, a shoulder at 190 °C and one additional smaller peak, whose reduction starts above 140 °C. On the one hand, the main peak is attributed to reduction of supported RuO_2 into metallic Ru [40–42], whereas the mentioned shoulder at lower temperature is due to reduction of well dispersed RuO_x species [43, 44]. Then, the peak at lowest temperature peak could be related to reduction of RuO_3, as already observed in XPS results.

From integration of H_2-TPR signal, total H_2 consumptions, RuO_3/RuO_2 ratios and H_2/Ru ratios were calculated and included in Table 3. RuO_3/RuO_2 ratios are between 0.17 and 0.24, i.e., all

catalysts present similar and considerably higher relative amounts of RuO_2 than of RuO_3. Finally, it should be noted that H_2/Ru molar ratios are between 2.2 and 2.3 (value slightly higher than required for RuO_2 reduction), which confirms the presence of RuO_2 and trace amounts of RuO_3, according to the following reduction step: $RuO_x + xH_2 \rightarrow Ru + xH_2O\ (x=2,3)$.

3.2. CO_2 methanation

The performance of catalysts was evaluated by analyzing CO_2 conversions and CH_4 yields. In all cases, CO was the only secondary product and carbon balance closed within ± 5%. The catalytic activity at different temperatures as a function of the Ni and Ru loading is shown in Figures 8a and 8b, respectively. First of all, as it can be clearly observed, the increase of metal content results in an enhancement of catalytic activity and, generally, a higher temperature provides a higher CO_2 conversion. However, slight decrease of CO_2 conversion is observed at temperatures above 400 °C in cases where conversions close to that of equilibrium are obtained, as expected for exothermic reactions. Regarding Ni/Al_2O_3 catalysts (Figure 8a), the onset temperature for CO_2 methanation is around 250 °C, the highest CO_2 conversions are achieved close to 450 °C for catalysts with Ni contents higher than 8% (X_{CO_2} ≈ 85%) and equilibrium CO_2 conversion is only reached above 475 °C for 20%Ni/Al_2O_3. Noteworthy, the temperature at which 50% CO_2 conversion is obtained (T_{50}) is reduced in 127 °C when increasing the Ni loading from 4 to 20% (T_{50} = 443 °C and T_{50} = 316 °C, respectively). In the same way, catalysts with Ni nominal loadings above 12% provide similar CO_2 conversion values (X_{CO_2} ≈ 80%) when reaction temperatures rises over 400 °C. Therefore, it can be concluded that 12% Ni loading and a metallic surface of 5.1 m^2 g^{-1} is sufficient to provide enough active sites (Ni^0) in order to achieve high CO_2 conversions at intermediate-high temperatures.

FIGURE 8

Analogously, Figure 8b shows the influence of temperature on catalytic performance of Ru/Al_2O_3 catalysts. In this case, higher CO_2 conversions are observed at low temperatures (T < 300 °C) in comparison with Ni based catalysts. Maximum CO_2 conversion is reached, regardless the Ru content, at 400 °C, being also around 85% for catalysts with high metal content. Taking into account that the variation of Ru loading is much lower, similar T_{50} reduction, as compared to Ni catalysts, is obtained: from 396 °C (1% Ru) to 310 °C (5% Ru). Note that, in line with Ni based catalysts, a higher metal loading provides greater activity and that the same saturation effect is observed, obtaining almost similar (or even lower) CO_2 conversions for catalysts with nominal Ru contents above 4% (metal surface of 0.61 m^2 g^{-1}). This is the minimum nominal content needed to achieve at least 80% CO_2 conversion above 350 °C. Hence, the impregnation of Ru

loading higher than 4% can be considered unnecessary, since no further enhancement in activity is observed.

In Figure 9, CH_4 yields of 12%Ni/Al_2O_3 and 4%Ru/Al_2O_3 catalysts are compared at 300, 350 and 400 °C. It can be noticed that increasing temperature leads to higher Y_{CH_4} (highest CH_4 productions are observed at 400 °C) and that 4%Ru/Al_2O_3 is notably more productive than 12%Ni/Al_2O_3 catalyst, in line with the upgrade in CO_2 conversions observed in Figure 8. In fact, regardless the studied temperature, Ru containing catalyst produces more methane than Ni based catalyst (35% vs. 15% at 300 °C, 80% vs. 55% at 350 °C and 85% vs. 77% at 400 °C). Noteworthy, CO yields lower than 1% were observed for 12%Ni/Al_2O_3 catalyst and negligible trace amounts of CO were produced by 4%Ru/Al_2O_3 catalyst.

FIGURE 9

The activity of alumina supported 12% Ni and 4%Ru catalysts was compared with other state-of-art materials recently reported in literature, including commercial samples [8, 18, 22, 24, 45, 46]. Table 4 includes the catalysts composition together with the main operational parameters, i.e. H_2/CO_2 molar ratio and W/F_{A0}. As can be observed, the main operational parameters differ from each other, and thus, the comparison is not straightforward. Although 12Ni/Al catalyst developed in this work presents a somewhat higher T_{50}, nickel loading is significantly lower with respect to other reported samples. Furthermore, the W/F_{A0} used in this study is the lowest, i.e. a lower amount of catalyst is used to treat the inlet feedstream. On the other hand, the 4Ru/Al sample developed in this work presents a similar T_{50} to that reported for other samples. Again, the T_{50} was evaluated in more demanding experimental conditions, with the lowest W/F_{A0}. Taking all this considerations into account, it can be concluded that the catalytic performance of Ni and Ru based catalysts prepared in this work is comparable to other state-of-art materials, including commercial samples.

TABLE 4

3.3. Activation energies and catalysts stability

To determine apparent activation energies in the absence of catalyst deactivation (no C deposition) the intermediate temperature region, from 275 to 335 °C, was chosen. Because differential reactor conditions were difficult to achieve at higher temperatures, the initial reaction rates approach was employed instead. Measurements of the catalytic performance at varying space-time (Figure 10a and 10b) allowed fitting conversion vs. space-time curves, which

its extrapolation at $W/F^0_{CO_2}=0$, and corresponding derivatives results in values of initial reaction rates at every temperature,

$$-r^0_{CO_2}=r_{CH_4}=\left(\frac{dX_{CO_2}}{d(W/F^0_{CO_2})}\right)_{W/F^0_{CO_2}=0}=k_{ap}\ f(C^0_{CO_2},C^0_{H_2}) \quad (5)$$

that together with the Arrhenius expression

$$k_{ap}=A_0\exp\left(-\frac{E_{ap}}{RT}\right) \quad (6)$$

$$\ln(-r^0_{CO_2})=\ln\left[A_0\ f(C^0_{CO_2},C^0_{H_2})\right]-\frac{E_{ap}}{R}\left(\frac{1}{T}\right) \quad (7)$$

allows determination of the apparent activation energy from the slope of linear plot of $\ln(-r^0_{CO_2})$ vs. $1/T$ (Equation 7), as represented in Figure 10c and 10d for 12%Ni/Al_2O_3 and 4%Ru/Al_2O_3, respectively.

FIGURE 10

With the aim of comparing activity of catalysts with different nature of the metal active phase, also turnover frequencies *(TOF)*, defined as an intrinsic reaction rate referred to molar surface metal active site (from H_2 chemisorption results, Table 2), have been calculated (Equation 8), resulting in values reported in Table 5.

$$TOF_{Me}\,(s^{-1})=\frac{-r^0_{CO_2},\ \text{mol}\ CO_2\ (\text{g cat.})^{-1}\ s^{-1}}{S_{Me},\ \text{mol Me (g cat.)}^{-1}} \qquad (\text{Me=Ni,Ru}) \quad (8)$$

Note that, disregarded of Ni or Ru catalysts, *TOF* increases exponentially with temperature, with one order of magnitude higher for Ru/Al_2O_3 than Ni/Al_2O_3 in the range of temperature from 275 to 300 °C. This clearly indicates that ruthenium is much more effective metal for CO_2 methanation than nickel.

TABLE 5

From these initial reaction rates values and applying Arrhenius equation, apparent activation energies were calculated for both formulations (Figure 10c and 10d). The apparent activation energy for CO_2 methanation resulted to be 129 kJ mol^{-1} over Ni/Al_2O_3 catalyst and 84 kJ mol^{-1} over Ru/Al_2O_3 catalyst. The determination of activation energy values has already been conducted by other authors, observing similar values that ranges 60-80 kJ mol^{-1} on Ru/Al_2O_3 catalysts [16, 20, 46] and 95-120 kJ mol^{-1} on Ni/Al_2O_3 catalysts [45, 48]. The observed notable

difference in activation energy (45 kJ mol^{-1}) is related to differences in reaction mechanism: it is known that noble metals are more effective in H_2 dissociation than non-noble and that may explain the lower activation energy observed for Ru/Al_2O_3. In fact, Dreyer et al. [47] have reported that the presence of H_2 adsorption sites is essential for efficient CH_4 formation.

Despite the high reaction heat of CO_2 methanation (ΔH = -165 kJ mol^{-1}), it should be noted that both Anderson criterion [49] and Mears criterion [50] were satisfied, indicating an absence of internal and external temperature gradients during catalytic runs for determination of activation energies (Table S1).

Finally, the stability of catalysts with the optimum metal contents ($12\%Ni/Al_2O_3$ and $4\%Ru/Al_2O_3$) was studied for 24h-on-stream at 350 °C. Interestingly, a slight increase in the CO_2 conversion was observed for $12\%Ni/Al_2O_3$ catalyst in Figure 11a. The CO_2 conversion of $4\%Ru/Al_2O_3$, in contrast, slightly decreased from 81.5 to 78.0% (Figure 11b). Ni and Ru based catalysts were characterized by TG and TEM after 24h-on-stream. Thermogravimetric studies carried out under $5\%O_2$/He flow showed no relevant mass losses when increasing temperature up to 850 °C (Figure S4), indicating that no carbon deposits were formed during stability tests at 350 °C and under a gas stream with high H_2 concentration. By means of TEM (Figure S5), average particle sizes of 6 and 7 nm were estimated for fresh and used Ni catalysts, respectively, which reveals a slight particle sintering during the stability test. The same conclusion was extracted for Ru based catalysts. The average particle size was 24 and 28 nm for fresh and used catalysts, respectively.

In the case of Ni based catalysts, the slight particle sintering seems to be compensated by the activation of additional nickel species and reduction of nickel oxide with high interaction with the alumina. On the other hand, as Ru is completely reduced before the catalytic test, the slight sintering of Ru particles results in a decrease of the CO_2 conversion during the stability test. It is worth to mention that in both cases the selectivity to methane kept stable, obtaining values higher than 98% (Figures 11c y 11d).

FIGURE 11

4. Conclusions

In this work, a series of alumina-supported Ni and Ru catalysts were prepared by wetness incipient impregnation varying the metal content, characterized by multiple techniques (N_2-physisorption, CO_2-TPD, XRD, XPS and H_2-TPR) and evaluated for CO_2 methanation. The main conclusions are listed as follows:

According to basicity results (CO_2-TPD), the impregnation of increasing loading of Ni and Ru results in the formation of new basic sites suggesting that both active phases are able to adsorb CO_2, which is an essential step in CO_2 methanation mechanism. Nevertheless, the different strength of those new basic sites indicates the presence of various species of adsorbed CO_2.

XRD results revealed that alumina supported Ru crystals tend to grow and agglomerate into larger particles with increasing of calcination temperature, resulting in lower metal dispersion. On the contrary, the increase of temperature does not affect Ni dispersion, but leads to the formation of nickel phases with higher interaction with alumina, especially for catalysts with low Ni content. According to H_2-chemisorption results, Ni dispersion decreases around 25% by increasing Ni content from 4 to 20% due to the formation of larger NiO particles. However, unlike for Ni/Al_2O_3 catalysts, the dispersion of Ru/Al_2O_3 catalysts is not significantly influenced by metal loading.

The reducibility of the active phase, linked to metal-support interaction, seemed to be a key factor. The reduction of alumina supported Ru is complete at low temperature (T < 300 °C), while alumina supported Ni is not completely reduced at 500 °C. This indicates that all Ru but not all Ni will be available to dissociate hydrogen during reaction. The reducibility is even lesser for catalysts with low Ni content due to a higher metal-support interaction, in accordance with XPS and H_2-TPR results.

Considering the saturation effect of CO_2 conversion with metal loading, $12\%Ni/Al_2O_3$ (T_{50} = 340 °C) and $4\%Ru/Al_2O_3$ (T_{50} = 310 °C) were the best formulations, providing maximum CO_2 conversions of 80 and 85% around 425 and 375 °C, respectively and being quite stable for 24h-on-stream. The TOF values for Ru/Al_2O_3 catalyst were considerably higher than those observed for Ni/Al_2O_3 at low temperature (T < 300 °C), since ruthenium is more effective in H_2 dissociation/adsorption than nickel, which is another fundamental step of reaction mechanism.

Acknowledgments

The support from the Economy and Competitiveness Spanish Ministry (CTQ2015-67597-C2-1-R and CTQ2015-67597-C2-2-R MINECO-FEDER), the Basque Government (IT657-13 and IT1297-19) and the SGIker (Analytical Services) at the University of the Basque Country are acknowledged. One of the authors (AQ) also acknowledges University of the Basque Country by his PhD grant (PIF-15/351).

References

[1] B. K. Sovacool, How long will it take? Conceptualizing the temporal dynamics of energy transitions. Energy Res. Soc. Sci. 13 (2016) 202–215.

[2] A. A. Olajire. Valorization of greenhouse carbon dioxide emissions into value-added products by catalytic processes. J. CO_2 Util. 3–4 (2013) 74–92.

[3] C. Song. Global challenges and strategies for control, conversion and utilization of CO_2 for sustainable development involving energy, catalysis, adsorption and chemical processing. Catal. Today 115 (2006) 2–32.

[4] W. Wang and J. Gong. Methanation of carbon dioxide: an overview. Front. Chem. Sci. Eng. 5(1) (2011) 2–10.

[5] F. Ocampo, B. Louis, A.-C. Roge. Methanation of carbon dioxide over nickel-based $Ce_{0.72}Zr_{0.28}O_2$ mixed oxide catalysts prepared by sol-gel method. Appl. Catal. A Gen. 369 (2009) 90–96.

[6] F. Ocampo, B. Louis, L. Kiwi-Minsker, A.-C. Roge. Effect of Ce/Zr composition and noble metal promotion on nickel based $Ce_xZr_{1-x}O_2$ catalysts for carbon dioxide methanation. Appl. Catal. A Gen. 392 (2011) 36–44.

[7] M. Romero-Sáez, L.Y. Jaramillo, W. Henao, U. de la Torre. Emerging Nanostructured Materials for Energy and Environmental Science (2018), Springer. http://dx.doi.org/10.1007/978-3-030-04474-9.

[8] G. Garbarino, D. Bellotti, P. Riani, L. Magistri, G. Busca. Methanation of carbon dioxide on Ru/Al_2O_3 and Ni/Al_2O_3 catalysts at atmospheric pressure: Catalysts activation, behavior and stability. Int. J. Hydrogen Energy 40 (2015) 9171–9182.

[9] S. Abate, C. Mebrahtu, E. Giglio, F. Deorsola, S. Bensaid, S. Perathoner, R. Pirone, G. Centi. Catalytic Performance of γ-Al_2O_3-ZrO_2-TiO_2-CeO_2 composite oxide supported Ni-Based Catalysts for CO_2 methanation. Ind. Eng. Chem. Res. 55 (2016) 4451–4460.

[10] X. Su, J. Xu, B. Liang, H. Duan, B. Hou, Y. Huang. Catalytic carbon dioxide hydrogenation to methane: A review of recent studies. J. Energy Chem. 25 (2016) 553–565.

[11] S. Rahmani, M. Rezaei, F. Meshkani. Preparation of promoted nickel catalysts supported on mesoporous nanocrystalline gamma alumina for carbon dioxide methanation reaction. J. Ind. Eng. Chem. (2014) 4176–4182.

[12] Q. Liu, F. Gu, X. Lu, Y. Liu, H. Li, Z. Zhong, G. Xu, F. Su. Enhanced catalytic performances of Ni/Al_2O_3 catalyst via addition of V_2O_3 for CO methanation. Appl. Catal. A Gen. 488 (2014) 37–47.

[13] D. Pandey, G. Deo. Effect of support on the catalytic activity of supported Ni-Fe catalysts for the CO_2 methanation reaction. J. Ind. Eng. Chem. 33 (2016) 99–107.

[14] F. Song, Q. Zhong, Y. Yu, M. Shi, Y. Wu, J. Hu, Y. Song. Obtaining well-dispersed Ni/Al_2O_3 catalyst for CO_2 methanation with a microwave-assisted method. Int. J. Hydrogen Energy 42 (2017) 4174–4183.

[15] D. Wierzbicki, R. Baran, R. Debek, M. Motak, T. Grzybek, M. E. Gálvez, P. Da Costa. The influence of nickel content on the performance of hydrotalcite-derived catalysts in CO_2 methanation reaction. Int. J. Hydrogen Energy 42 (2017) 23548–23555.

[16] J. H. Kwak, L. Kovarik, J. Szanyi. CO_2 reduction on supported Ru/Al_2O_3 catalysts: cluster size dependence of product selectivity. ACS Catal. 3 (2013) 2449–2455.

[17] C. Janke, M.S. Duyar, M. Hoskins, R. Farrauto. Catalytic and adsorption studies for the hydrogenation of CO_2 to methane. Appl. Catal. B Environ. 152–153 (2014) 184–191.

[18] S. Tada, O. J. Ochieng, R. Kikuchi, T. Haneda, H. Kameyama. Promotion of CO_2 methanation activity and CH_4 selectivity at low temperatures over $Ru/CeO_2/Al_2O_3$ catalysts. Int. J. Hydrogen Energy 39 (2014) 10090–10100.

[19] S. Toemen, W. A. W. Abu Bakar, R. Ali. Effect of ceria and strontia over $Ru/Mn/Al_2O_3$ catalyst: Catalytic methanation, physicochemical and mechanistic studies. J. CO_2 Util. 13 (2016) 38–49.

[20] G. Garbarino, D. Bellotti, E. Finocchio, L. Magistri, G. Busca. Methanation of carbon dioxide on Ru/Al_2O_3: Catalytic activity and infrared study. Catal. Today 277 (2016) 21–28.

[21] A. Quindimil, U. De-La-Torre, B. Pereda-Ayo, José A. González-Marcos, Juan R. González-Velasco. Ni catalysts with La as promoter supported over Y- and BETA- zeolites for CO_2 methanation. Appl. Catal. B Environ. 218 (2018) 393–403.

[22] G. Garbarino, C. Wang, T. Cavattoni, E. Finocchio, P. Riani, M. Flytzani-Stephanopoulos, G. Busca. A study of Ni/La-Al2O3 catalysts: A competitive system for CO_2 methanation. Appl. Catal. A Gen. 248 (2019) 286-297.

[23] I. Iglesias, A. Quindimil, F. Mariño, U. De-La-Torre, Juan R. González-Velasco. Zr promotion effect in CO_2 methanation over ceria supported nickel catalysts. Int. J. Hydrogen Energy 44 (2019) 1710-1719.

[24] R. Daroughegi, F. Meshkani, M. Rezaei. Enhanced activity of CO_2 methanation over mesoporous nanocrystalline $Ni-Al_2O_3$ catalysts prepared by ultrasound-assisted co-precipitation method. Int. J. Hydrogen Energy 42 (2017) 15115–15125.

[25] D. Wierzbicki, R. Debek, M. Motak, T. Grzybek, M. E. Gálvez, P. Da Costa. Novel Ni-La-hydrotalcite derived catalysts for CO_2 methanation. Catal. Commun. 83 (2016) 5–8.

[26] R. Debek, M. Radlik, M. Motak, M. E. Galvez, W. Tureik, P. Da Costa, T. Grzybek. Ni-containing Ce-promoted hydrotalcite derived materials as catalysts for methane reforming with carbon dioxide at low temperature – On the effect of basicity. Catal. Today 257 (2015) 59–65.

[27] Z. Boukha, C. Jiménez-González, M. Gil-Calvo, B. de Rivas, J.R. González-Velasco, J. I. Gutiérrez-Ortiz, R. López-Fonseca. $MgO/NiAl_2O_4$ as a new formulation of reforming catalysts: Tuning the surface properties for the enhanced partial oxidation of methane. Appl. Catal. B Environ. 199 (2016) 372–383.

[28] Z. Boukha, C. Jiménez-González, B de Rivas, J.R. González-Velasco, J. I. Gutiérrez-Ortiz, R. López-Fonseca. Synthesis, characterization and performance evaluation of spinel-derived Ni/Al_2O_3 catalysts for various methane reforming reactions. Appl. Catal. B Environ. 158–159 (2014) 190–201.

[29] E. Heracleous, A.F. Lee, K. Wilson, A.A. Lemonidou. Investigation of Ni-based alumina-supported catalysts for the oxidative dehydrogenation of ethane to ethylene: structural characterization and reactivity studies. J. Catal. 231 (2005) 159–171.

[30] Hui Li, Hexing Li, Wei-Lin Dai, Weijiang Wang, Zhigang Fang, Jing-Fa Deng. XPS studies on surface electronic characteristics of Ni–B and Ni–P amorphous alloy and its correlation to their catalytic properties. Appl. Surf. Sci. 152 (1999) 25–34.

[31] C. Heine, B. A. J. Lechner, H. Bluhm, M. Salmeron. Recycling of CO: Probing the chemical state of the Ni(111) surface during the methanation reaction with ambient pressure X-ray photoelectron spectroscopy. J. Am. Chem. Soc. 138(40) (2016) 13246–13252.

[32] H.-W. Kim, K.-M. Kang, H.-Y. Kwak, J. H. Kim. Preparation of supported Ni catalysts on various metal oxides with core/shell structures and their tests for the steam reforming of methane. Chem. Eng. J. 168 (2011) 775–783.

[33] C. Jiménez-González, Z. Boukha, B. de Rivas, J. J. Delgado, M. A. Cauqui, J. R. González-Velasco, J. I. Gutiérrez-Ortiz, R. López-Fonseca. Structural characterisation of Ni/alumina reforming catalysts activated at high temperature. Appl. Catal. A Gen. 466 (2013) 9–20.

[34] K.S. Kim and N. Winograd. X-ray photoelectron spectroscopic studies of ruthenium-oxygen surfaces. J. Catal. 35 (1974) 66–72.

[35] S. Kawi, S. Y. Liu, S.-C. Shen. Catalytic decomposition and reduction of N_2O on Ru/MCM-41 catalyst. Catal. Today 68 (2001) 237–244.

[36] K. Qadir, S. H. Joo, B. S. Mun, D. R. Butcher, J. R. Renzas, F. Aksoy, Z. Liu, G. A. Somorjai, J. Y. Park. Intrinsic relation between catalytic activity of CO oxidation on Ru nanoparticles and Ru oxides uncovered with ambient pressure XPS. Nano Lett. 12 (2012) 5761–5768.

[37] S. Carenco, C. Sassoye, M. Faustini, P. Eloy, D. P. Debecker, H. Bluhm, M. B. Salmeron. The Active State of Supported Ruthenium Oxide Nanoparticles during Carbon Dioxide Methanation. J. Phys. Chem. C 120(28) (2016) 15354–15361.

[38] A. Morales-Marín, J.L. Ayastuy, U. Iriarte-Velasco, M.A. Gutierrez-Ortiz. Nickel aluminate spinel-derived catalysts for the aqueous phase reforming of glycerol: Effect of reduction temperature. Appl. Catal. B Environ. 244 (2019) 931–945.

[39] K. Ray, G. Deo. A potential descriptor for the CO_2 hydrogenation to CH_4 over Al_2O_3 supported Ni and Ni-based alloy catalysts. Appl. Catal. B Environ. 218 (2017) 525–537.

[40] P. Betancourt, A. Rives, R. Hubaut, C.E. Scott, J. Goldwasser. A study of the ruthenium-alumina system. Appl. Catal. A Gen. 170 (1998) 307–314.

[41] V. Mazzieri, F. Coloma-Pascual, A Arcoya, P.C. L'Argentière, N.S. Fígoli. XPS, FTIR and TPR characterization of Ru/Al_2O_3 catalysts. Appl. Surf. Sci. 210 (2003) 222–230.

[42] T. Mitsui, K. Tsutsui, T. Matsui, R. kikuchi, K. Eguchi. Support effect on complete oxidation of volatile organic compounds over Ru catalysts. Appl. Catal. B Environ. 81 (2008) 56–63.

[43] R. Lanza, S. G. Jaras, P. Canu. Partial oxidation of methane over supported ruthenium catalysts. Appl. Catal. A Gen. 325 (2007) 57–67.

[44] K. Kousi, D.I. Kondarides, X.E. Verykios, C. Papadopoulou. Glycerol steam reforming over modified Ru/Al_2O_3 catalysts. Appl. Catal. A Gen. 542 (2017) 201–211.

[45] C. V. Miguel, A. Mendes, L.M. Madeira. Intrinsic kinetics of CO_2 methanation over an industrial nickel-based catalyst. J. CO_2 Util. 25 (2018) 128–136.

[46] L. Falbo, M. Martinelli, C. G. Visconti, L. Lietti, C. Bassano, P. Deiana. Kinetics of CO_2 methanation on a Ru-based catalyst at process conditions relevant for Power-to-Gas applications. Appl. Catal. B Environ. 225 (2018) 354-363.

[47] J. H. A. Dreyer, P. Li, L. Zhang, G. K. Beh, R. Zhang, P. H.-L. Sit, W. Y. Teoh. Influence of the oxide support reducibility on the CO_2 methanation over Ru-based catalysts. Appl. Catal. B Environ. 219 (2017) 715–726.

[48] T. Van Herwijnen, H. Van Doesburg, W.A. De Jong. Kinetics of the methanation of CO and CO_2 on a nickel catalyst. J. Catal. 28 (1973) 391–402.

[49] J.B. Anderson. A criterion for isothermal behavior of catalyst pellet. Chem. Eng. Sci. 18 (1963) 147-148.

[50] D. E. Mears. Tests for transport limitations in experimental catalytic reactors. Ind. Eng. Chem. Proc. Des. Dev. 10 (1971) 541-547.

Figure 1. CO_2-TPD profiles of γ-Al_2O_3 support, 20%Ni/Al_2O_3 and 5%Ru/Al_2O_3 catalysts.

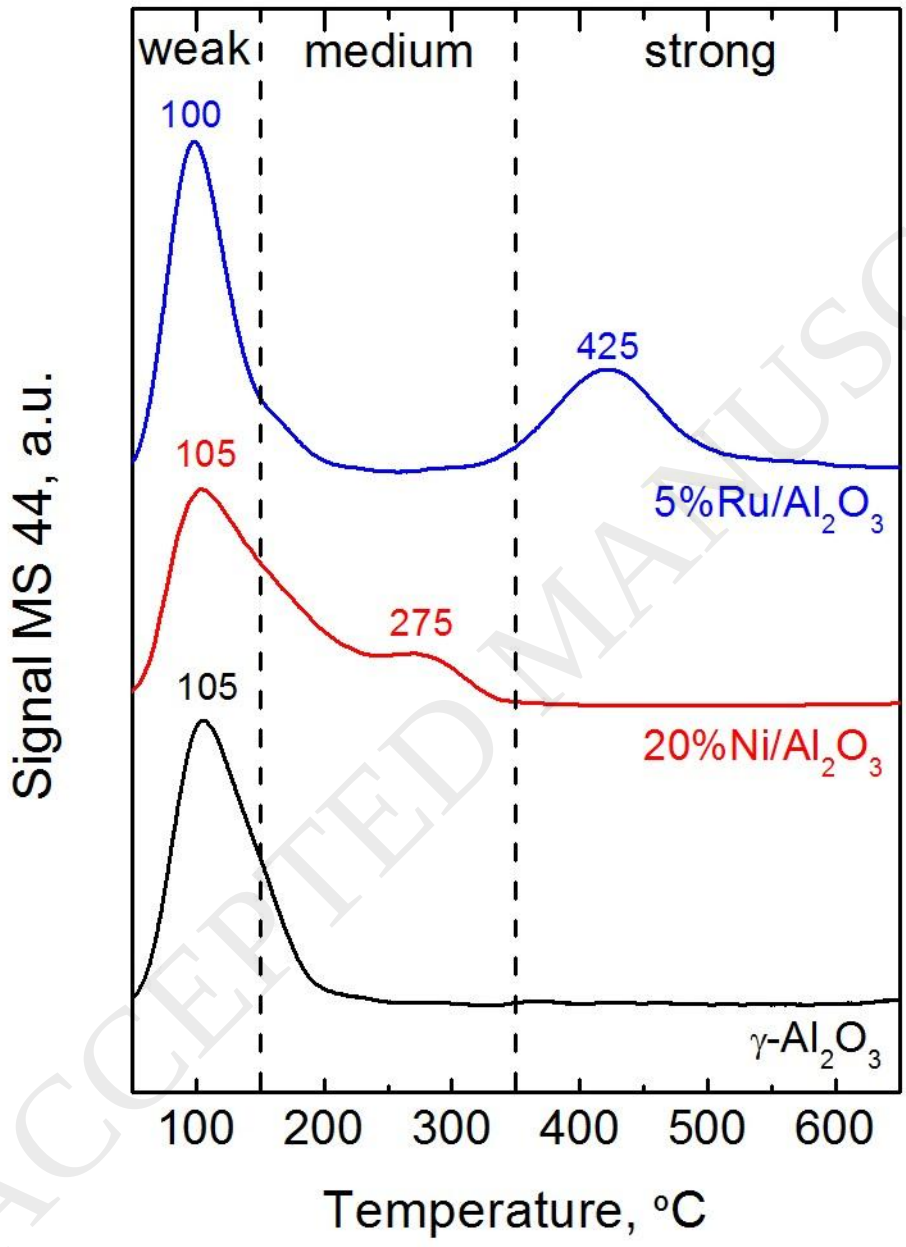

Figure 2. XRD patterns of reduced (a) alumina-supported Ni catalysts and (b) alumina-supported Ru catalysts.

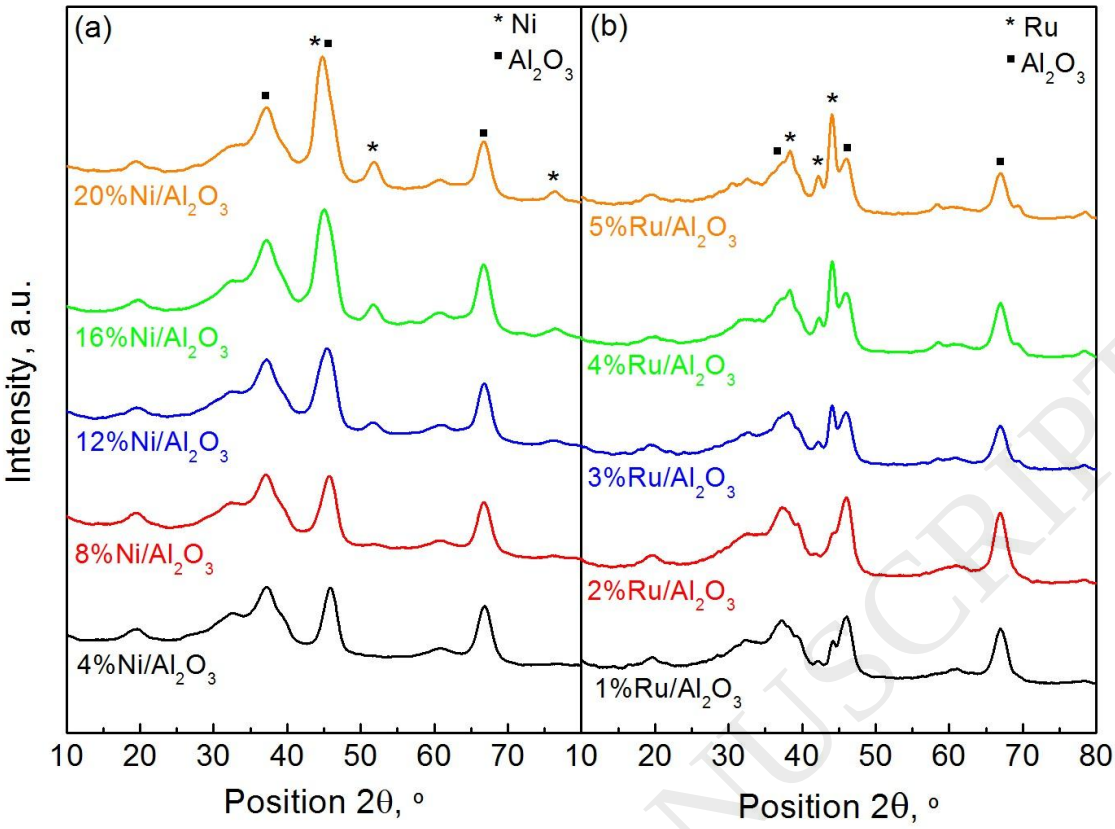

Figure 3. Thermodiffractometric analysis of (a) 12%$NiAl_2O_3$ and (b) 4%Ru/Al_2O_3 catalysts from 30 to 1010 °C.

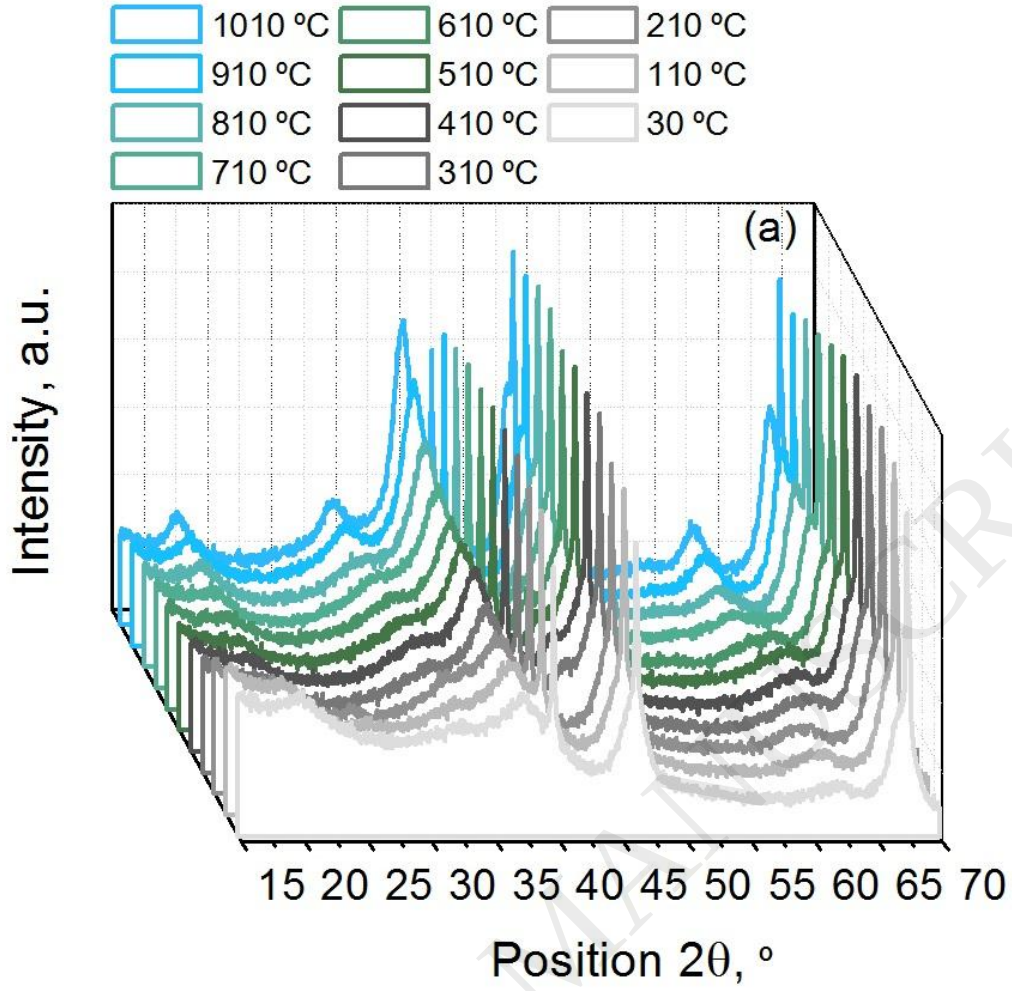

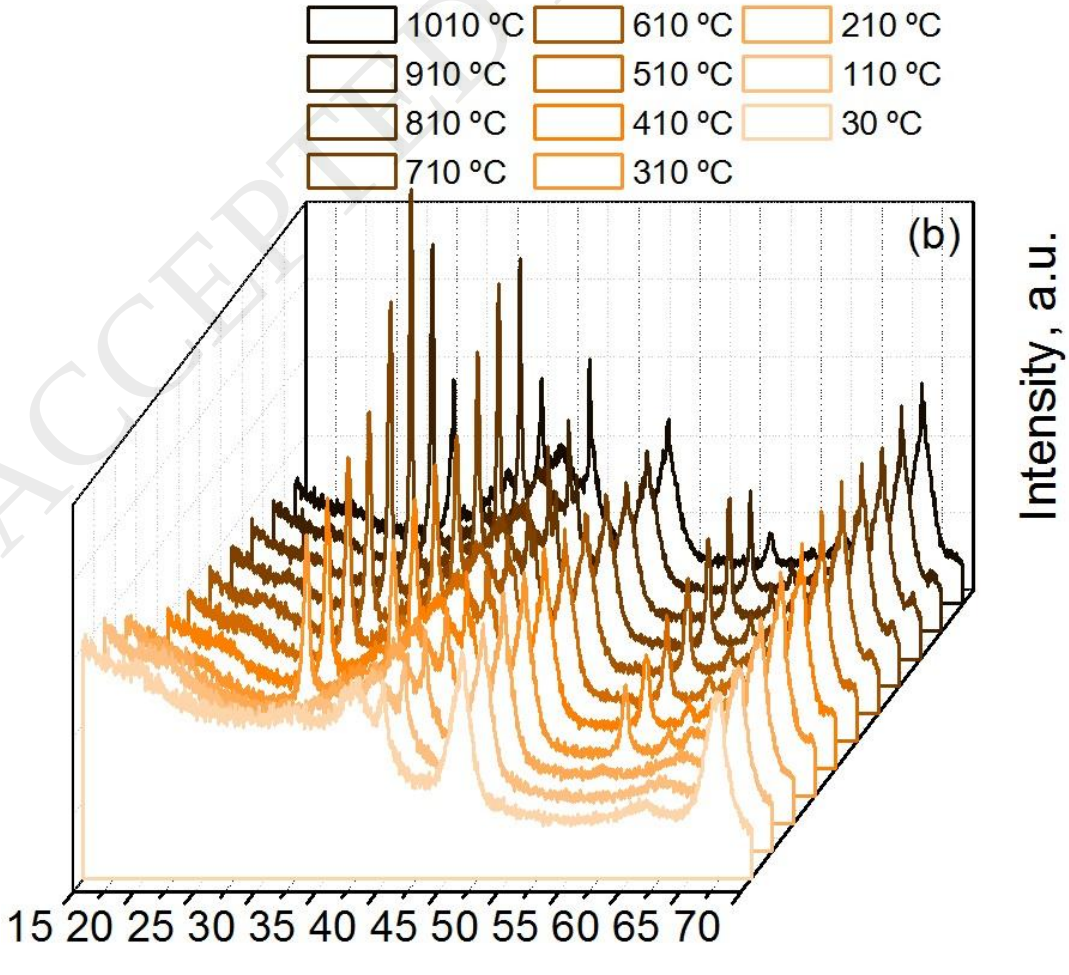

Figure 4. Effect of (a) Ni and (b) Ru content on Ru/Al and Ni/Al surface atomic ratios.

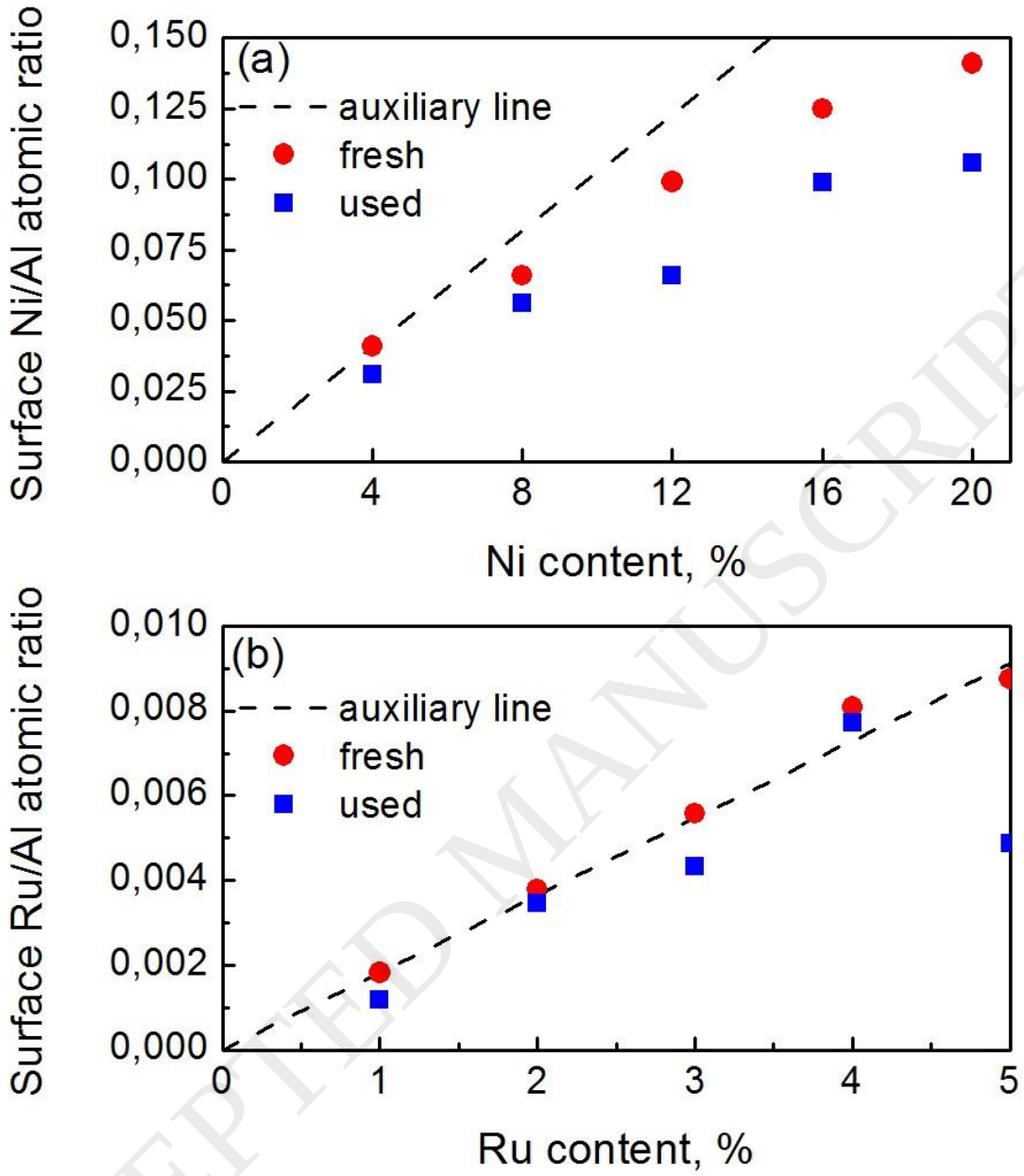

Figure 5. Ni $2p_{3/2}$ XPS spectra of (a) fresh and (b) used catalysts.

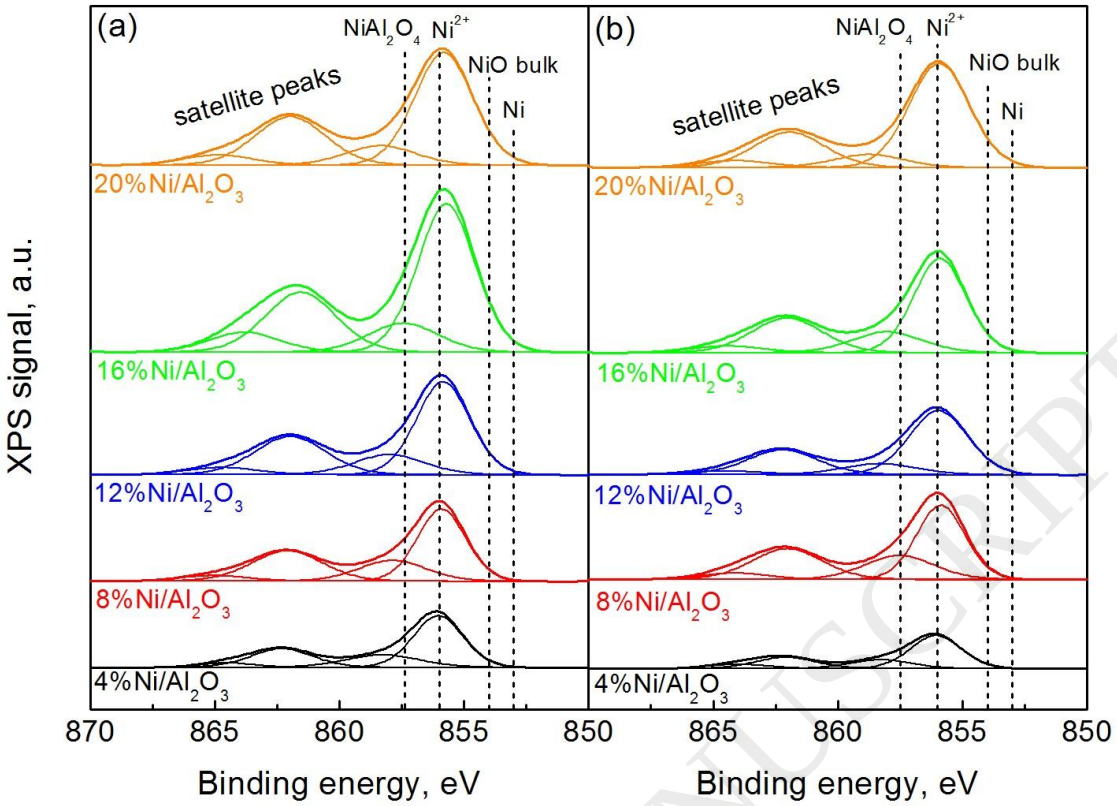

Figure 6. Ru $2d_{5/2}$ XPS spectra of (a) fresh and (b) used catalysts.

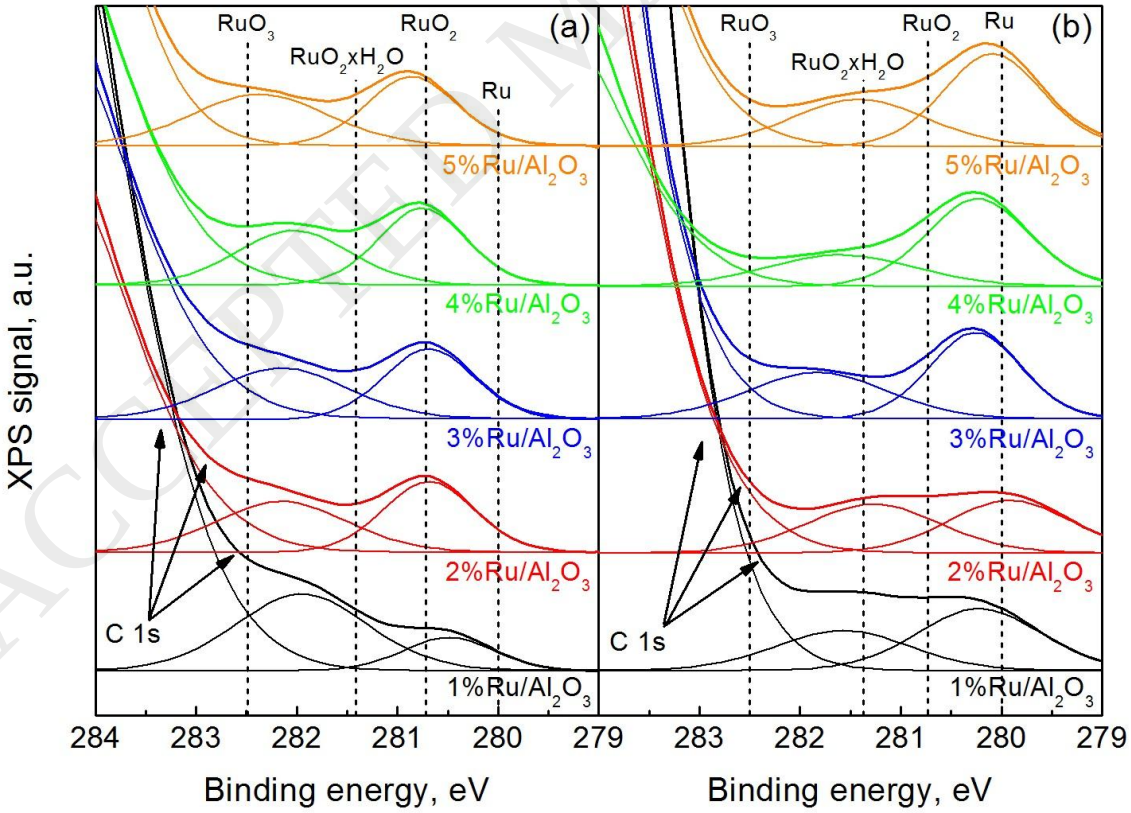

Figure 7. H_2-TPR profiles of (a) Ni/Al_2O_3 catalysts and (b) Ru/Al_2O_3 catalysts.

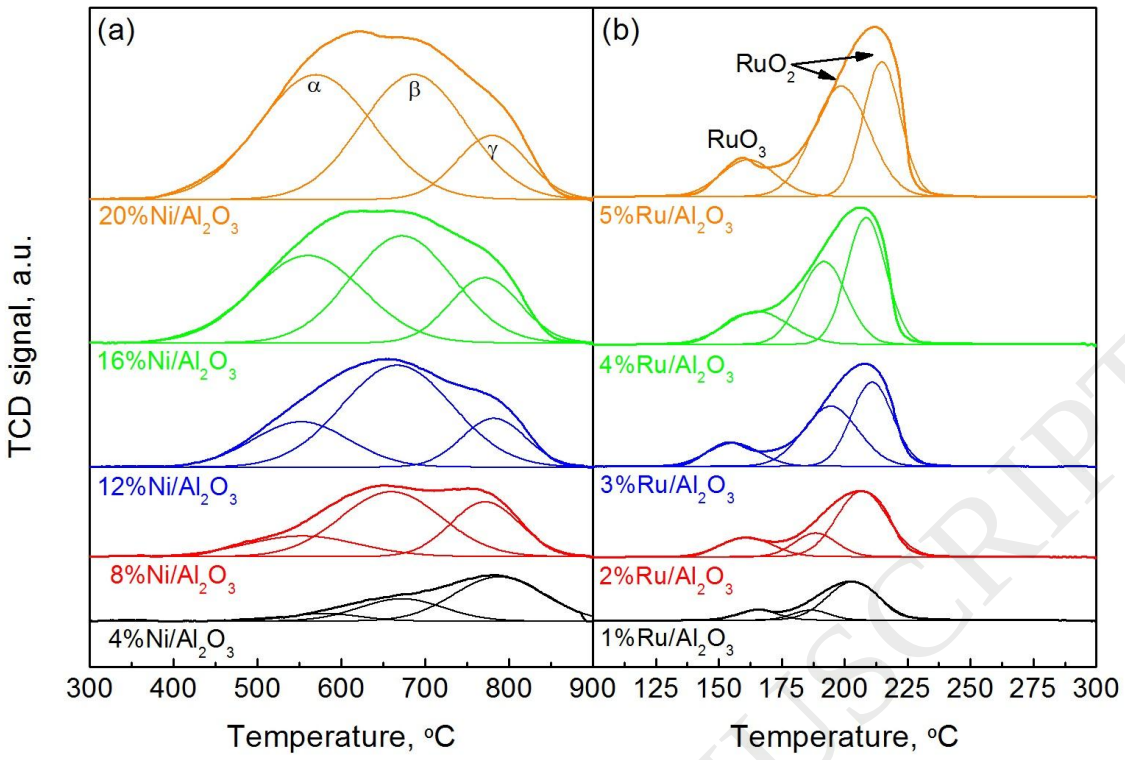

Figure 8. CO_2 conversion as a function of reaction temperature for (a) Ni/Al_2O_3 and (b) Ru/Al_2O_3 catalysts.

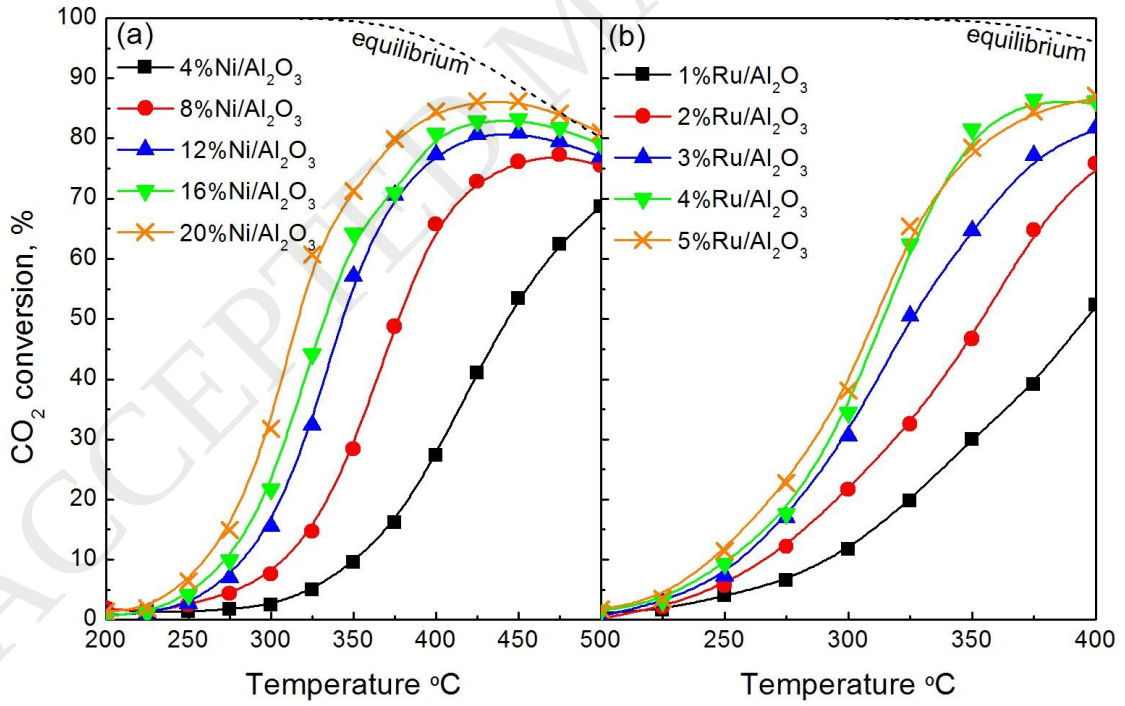

Figure 9. C-species distribution of $12\%Ni/Al_2O_3$ and $4\%Ru/Al_2O_3$ catalysts at 300, 350 and 400 °C.

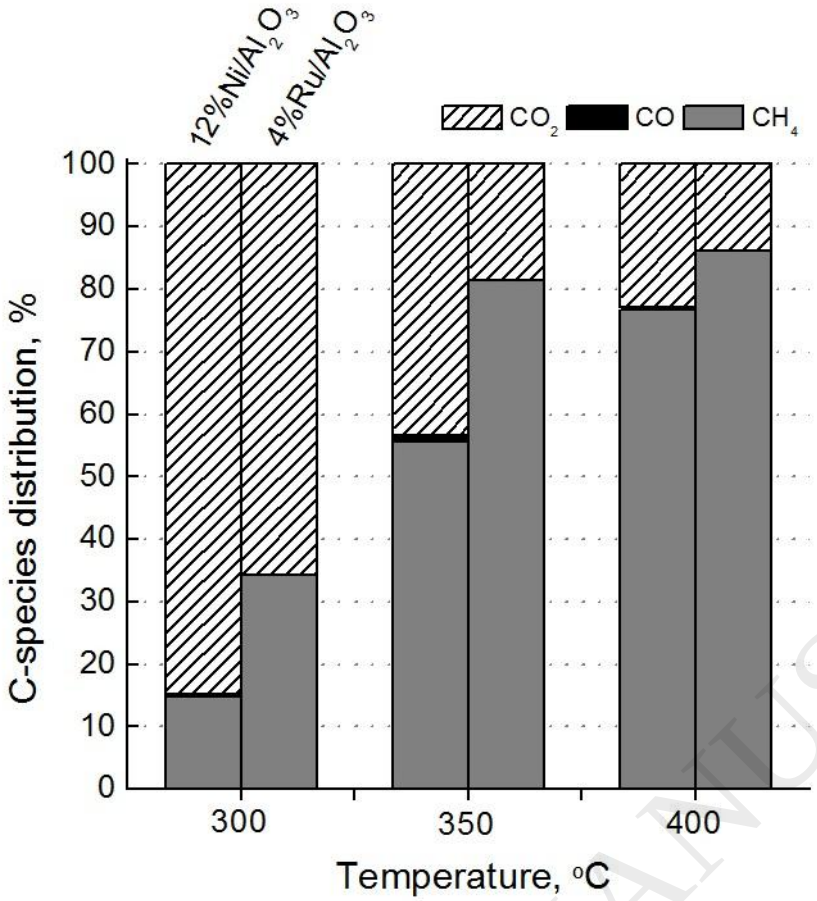

Figure 10. Effect of W/F_{A0} on CO_2 conversion for (a) 12%Ni/Al_2O_3 and (b) 4%Ru/Al_2O_3 catalysts together with Arrhenius plots (c and d).

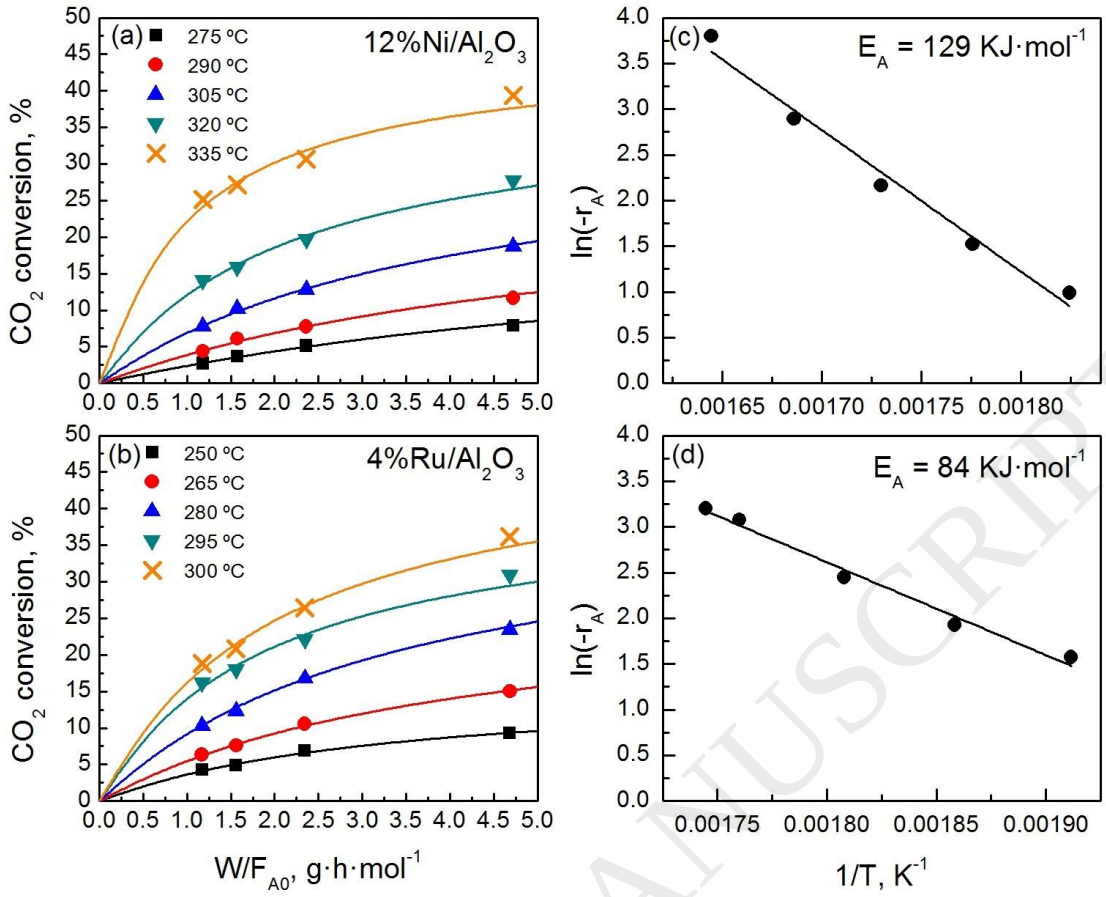

Figure 11. Evolution of CO_2 conversion and selectivity to CH_4/CO at 350 °C with time-on-stream over 24h for (a) 12%Ni/Al_2O_3 and (b) 4%Ru/Al_2O_3 catalysts.

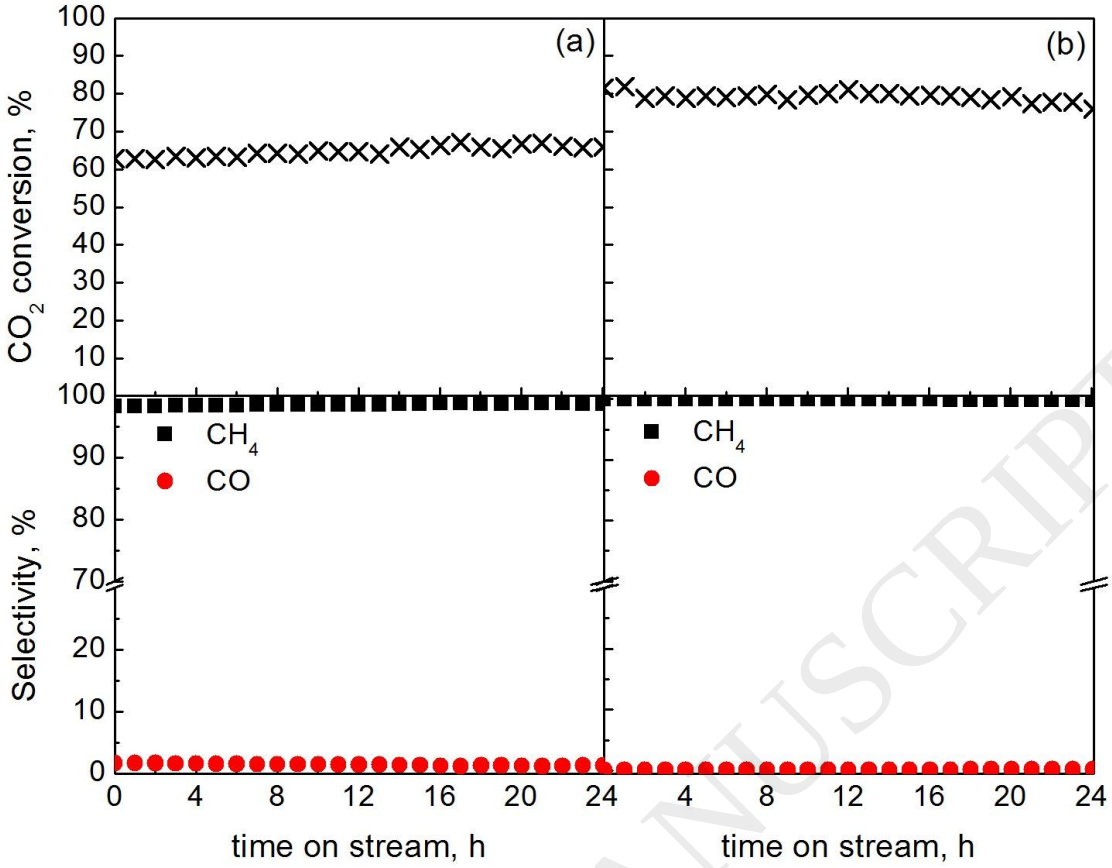

TABLES AND FIGURES CAPTIONS

Table 1. Physicochemical properties of alumina-supported Ni and Ru catalysts.

Table 2. Crystallite sizes and metal dispersions of the catalysts.

Table 3. Data from H_2-TPR studies of the impregnated Ni and Ru catalysts.

Table 4. Catalytic performance comparison among Ni and Ru based catalysts reported in literature.

Table 5. Initial reaction rates and TOF values of 12%Ni/Al_2O_3 and 4%Ru/Al_2O_3 catalysts.

TABLE 1

Sample	Ni/Al and Ru/Al[a]	S_{BET} (m^2 g^{-1})	V_{meso} (cm^3 g^{-1})	d_{pore} (nm)	Desorbed CO_2[b], µmol g^{-1}	Basicity (µmol CO_2 m^{-2})
Al_2O_3	-	214	0.563	10.1	69	0.32
4%Ni/Al_2O_3	0.038	191	0.435	8.8	80	0.42
8%Ni/Al_2O_3	0.079	175	0.383	8.4	72	0.41
12%Ni/Al_2O_3	0.122	160	0.373	9.0	71	0.44
16%Ni/Al_2O_3	0.175	147	0.369	9.7	68	0.46

20%Ni/Al_2O_3	0.224	131	0.326	9.6	65	0.50
1%Ru/Al_2O_3	0.007	198	0.411	8.0	71	0.36
2%Ru/Al_2O_3	0.015	193	0.429	8.4	74	0.38
3%Ru/Al_2O_3	0.021	185	0.417	8.5	69	0.37
4%Ru/Al_2O_3	0.029	172	0.382	8.5	67	0.39
5%Ru/Al_2O_3	0.032	179	0.425	9.1	75	0.42

[a] Determined by XRF.

[b] Calculated from CO_2-TPD profiles.

TABLE 2

Catalyst	Crystallite size (nm)[a]		Dispersion (%)[b]	Metal surface ($m^2\ g^{-1}$)
	NiO or RuO_2	**Ni or Ru**		
4%Ni/Al_2O_3	< 5	< 5	38.3	0.985
8%Ni/Al_2O_3	< 5	< 5	26.1	2.907
12%Ni/Al_2O_3	< 5	4.8	17.9	5.083
16%Ni/Al_2O_3	9	6.1	13.3	6.186
20%Ni/Al_2O_3	8.5	7.3	11.0	7.527
1%Ru/Al_2O_3	29.0	7.4	5.5	0.201
2%Ru/Al_2O_3	34.0	8.1	4.7	0.344
3%Ru/Al_2O_3	37.9	11.0	4.5	0.489
4%Ru/Al_2O_3	41.4	11.3	4.2	0.609
5%Ru/Al_2O_3	43.8	12.1	3.9	0.711

[a]Estimated by Scherrer equation.
[b]Calculated by H_2-chemisorption.

TABLE 3

Catalyst	Total H_2 uptake (mmol g^{-1})	Ni Cont.[a] (wt.%)	Species (%)			H_2/Ni	Reducibility[b] (%)
			α	β	γ		
4%Ni/Al_2O_3	0.65	3.8	8	30	62	1.01	10
8%Ni/Al_2O_3	1.26	7.4	18	52	30	0.97	22
12%Ni/Al_2O_3	1.86	10.9	23	60	17	0.97	38
16%Ni/Al_2O_3	2.52	14.8	38	44	18	0.99	47
20%Ni/Al_2O_3	3.16	18.5	45	41	14	1.01	56
Catalyst	**Total H_2 uptake (mmol g^{-1})**	**Ru Cont. (%)**	**RuO_3/RuO_2 ratio**			**H_2/Ru**	**Reducibility (%)**
1%Ru/Al_2O_3	0.23	1.1	0.17			2.32	100
2%Ru/Al_2O_3	0.45	2.1	0.23			2.27	100
3%Ru/Al_2O_3	0.66	3.1	0.18			2.22	100
4%Ru/Al_2O_3	0.93	4.3	0.24			2.35	100
5%Ru/Al_2O_3	1.08	5.1	0.18			2.18	100

[a]Determined from integration of H_2-TPR profiles.
[b]Reduction conditions: 500 °C for 1h under 20%H_2/Ar. For these calculations Ni(II) has been assumed.

TABLE 4

Composition	Description	H_2/CO_2 ratio	$W / F^0_{CO_2}$ (g h mol^{-1})	T_{50}, °C	Reference
12Ni/Al	Incipient wetness impregnation	5	5	340	This work
25NiO/Ca-Al	Comercial (METH134)	4	6	325	[45]
25Ni-Al	Co-precipitation	3.5	11	300	[24]
17NiO/14La/Al	Incipient wetness impregnation	5	8	280	[22]
4Ru/Al	Incipient wetness impregnation	5	5	310	This work
0.5Ru/Al	Commercial	4	25	300	[46]
3Ru/Al	Commercial	5	7	365	[8]
2Ru/30Ce/Al	Wet impregnation	4	11	285	[18]

TABLE 5

Catalyst	Temperature (°C)	$-r^0_{CO_2}$ (mmol h^{-1} g^{-1})	*TOF* (s^{-1})
$12\%Ni/Al_2O_3$	275	27	0.06
	290	46	0.1
	305	87	0.19
	320	181	0.39
	335	446	0.95
$4\%Ru/Al_2O_3$	250	48	0.81
	265	69	1.16
	280	116	1.95
	295	217	3.65
	300	246	4.14